

## RESEARCH ARTICLE

# Long-axis rotation: a missing degree of freedom in avian bipedal locomotion

Robert E. Kambic\*, Thomas J. Roberts and Stephen M. Gatesy

**ABSTRACT**

Ground-dwelling birds are typically characterized as erect bipeds having hind limbs that operate parasagittally. Consequently, most previous research has emphasized flexion/extension angles and moments as calculated from a lateral perspective. Three-dimensional (3D) motion analyses have documented non-planar limb movements, but the skeletal kinematics underlying changes in foot orientation and transverse position remain unclear. In particular, long-axis rotation of the proximal limb segments is extremely difficult to measure with topical markers. Here, we present six degree of freedom skeletal kinematic data from maneuvering guineafowl acquired by marker-based XROMM (X-ray Reconstruction of Moving Morphology). Translations and rotations of the hips, knees, ankles and pelvis were derived from animated bone models using explicit joint coordinate systems. We distinguished sidesteps, sidestep yaws, crossover yaws, sidestep turns and crossover turns, but birds often performed a sequence of blended partial maneuvers. Long-axis rotation of the femur (up to 38 deg) modulated the foot's transverse position. Long-axis rotation of the tibiotarsus (up to 65 deg) also affected medio-lateral positioning, but primarily served to either re-orient a swing phase foot or yaw the body about a stance phase foot. Tarsometatarsal long-axis rotation was minimal, as was hip, knee and ankle abduction/adduction. Despite having superficially hinge-like joints, birds coordinate substantial long-axis rotations of the hips and knees to execute complex 3D maneuvers while striking a diversity of non-planar poses.

**KEY WORDS:** Locomotion, Bipedalism, Kinematics, Avian, XROMM, Three-dimensional, Guinea fowl, X-ray, Animation

**INTRODUCTION**

Comparative anatomy textbooks typically distinguish two basic types of tetrapod limb posture. 'Sprawling' forms are portrayed as having laterally abducted limbs that move in a complex three dimensional (3D) pattern, whereas 'erect' forms are said to tuck their limbs under the body and operate parasagittally. Birds are considered erect, and most functional studies of avian bipedalism reflect this planar perspective. Whole-limb kinematics (Gatesy and Biewener, 1991; Abourachid and Renous, 2000; Verstappen et al., 2000; Abourachid, 2001) and whole-body kinetics (Roberts and Scales, 2002; Henry et al., 2005; Daley and Biewener, 2006; Hancock et al., 2007; Birn-Jeffery and Daley, 2012; Andrada et al., 2013a) are typically studied with lateral film or video records. Likewise, analyses of joint rotation are usually restricted to flexion/extension (FE) angles (Sigmund, 1959; Cracraft, 1971;

Rylander and Bolen, 1974; Jacobson and Hollyday, 1982; Manion, 1984; Gatesy, 1990; Gatesy, 1999; Johnston and Bekoff, 1992; Abourachid and Renous, 2000; Reilly, 2000; Verstappen et al., 2000; Ellerby and Marsh, 2010; Smith et al., 2010; Nyakatura et al., 2012). Given the relatively small transverse component of the ground reaction force during forward locomotion (Clark and Alexander, 1975; Main and Biewener, 2007; Troy et al., 2009), inverse dynamic studies normally emphasize net FE joint moments as well (Roberts, 2001; Roberts and Scales, 2004; Daley et al., 2007; Rubenson and Marsh, 2009; Andrada et al., 2013b). Our current perception of bird hind limbs thus remains deeply rooted in the erect paradigm.

But what if a two-dimensional (2D) model is insufficient for fully understanding the musculoskeletal morphology, mechanics, motor control and evolutionary history of avian bipeds? Although ground-dwelling birds (e.g. galliforms, ratites, tinamous) are commonly offered as classic examples of erect tetrapods, kinematic data paint a more complex picture. Studies of ostriches (Jindrich et al., 2007; Rubenson et al., 2007) and emus (Goetz et al., 2008) using multiple cameras to track surface markers were the first to measure the 3D complexity of avian bipedalism. Hind limb segments were neither parasagittal nor planar during walking, running and cutting maneuvers. Subsequent 3D analyses using X-ray imaging of the skeleton confirmed these results for smaller species (Abourachid et al., 2011; Hugel et al., 2011; Provini et al., 2012; Stoessel and Fischer, 2012).

The non-planar nature of avian hind limbs should be expected given anatomical constraints and functional demands. Tetrapods, as bilaterally symmetrical organisms, lack midline limbs projecting directly beneath the body's center of mass. In order to stand stably on one leg, even the most narrow-bodied biped must configure its limb segments to span from a laterally offset hip joint to a more medially placed center of pressure. Such a limb might theoretically operate within an inclined plane during forward locomotion, but the requirements of turning and maneuvering stipulate an expansion of its workspace (Jindrich et al., 2007). Therefore, a full consideration of joint function necessitates analysis of maneuvering and other behaviors in addition to steady forward motion. A terrestrial bird must be able to displace its center of mass transversely as well as yaw to change direction, but how do avian hind limbs accomplish these 3D tasks?

An increase in limb workspace might entail additional rotational degrees of freedom (d.f.) at one or more joints. Segments could be moved away from or towards the midline by abduction/adduction (ABAD) or reoriented by long-axis rotation (LAR). Given avian joint geometry, ABAD may be a less likely candidate than LAR. At the hip, the projecting pelvic antitrochanter likely limits femoral abduction (Hutchinson and Gatesy, 2000; Hertel and Campbell, 2007; Troy et al., 2009), whereas the body constrains femoral adduction. ABAD at the bicondylar knee and intertarsal (ankle) joints would tend to disarticulate one condyle and cause instability. However, some amount of ABAD and LAR has been reported at all

Department of Ecology and Evolutionary Biology, Brown University, RI 02912, USA.

\*Author for correspondence (Robert\_kambic@brown.edu)

Received 17 December 2013; Accepted 9 May 2014

**List of abbreviations**

ABAD	abduction/adduction
ACS	anatomical coordinate system
d.f.	degree(s) of freedom
FE	flexion/extension
JCS	joint coordinate system
LAR	long-axis rotation

of these joints in running ostriches (Rubenson et al., 2007). Our goal was to measure how birds coordinate rotational d.f. within joints, among joints and among limbs to perform non-sagittal movements.

Herein, we describe results of a 3D kinematic analysis of avian bipedal locomotion. To specifically explore the role of LAR in limb movement, we used biplanar X-ray imaging to record helmeted guineafowl, *Numida meleagris* (Linnaeus 1758), executing sidesteps, yaws and sharp turns. The position and orientation of the pelvis, femora, tibiotarsi and tarsometatarsi were reconstructed using marker-based XROMM [X-ray Reconstruction of Moving Morphology (Brainerd et al., 2010; Gatesy et al., 2010)]. Animated bone models allowed high-resolution measurement of six d.f. skeletal kinematics using explicit joint coordinate systems. We predicted that the hip, knee and ankle joints are not simple hinges restricted to FE, and that LAR is responsible for expanding the limb's workspace during avian bipedal locomotion.

**RESULTS****Types of maneuvers**

After reviewing all of the recorded maneuvering trials ( $N=77$ ), we identified repeatable patterns of limb/body movement. We distinguished three broad categories of maneuvers (Fig. 1; supplementary material Movie 1): sidesteps, yaws and turns. Sidesteps were characterized by transverse displacement with little

pelvic rotation, whereas yaws predominantly entailed reorienting the body from a standing start. Turns involved both reorientation and displacement while moving forward. Following Jindrich and colleagues (Jindrich et al., 2006; Jindrich et al., 2007), we further differentiated turns and yaws as either sidestep or crossover. In sidestep maneuvers, the swing limb moved laterally away from the stance limb, thereby spreading the feet. In crossover maneuvers, the swing limb moved medially and often passed in front of the stance foot. Thus, for yaws and turns, the stance foot was on the outside of the arc in sidesteps and on the inside of the arc in crossovers.

The following sections describe XROMM data exemplifying these five maneuvers. For clarity, we sought examples of complete, 'clean' maneuvers rather than partial elements. Because our goal was to quantify the relative contribution of rotational d.f. to maneuvering locomotion, we chose trials with relatively large limb excursions over smaller maneuvers in which the underlying skeletal kinematics were more subtle. To foster comparison, we show examples in which all birds sidestepped, yawed and turned to the right. We address a more complex sequence and variation within maneuvers in the final subsection of Results.

**Sidesteps**

Complete sidestep maneuvers can be divided into three phases (Fig. 2A) based on foot and body movement. During the 'split' phase, the lead limb is lifted and moved laterally (Fig. 2A, frames 1–2). In the 'shift' phase, the bird continues its transverse movement while keeping both feet planted (Fig. 2A, frames 2–3). Finally, the trailing limb is lifted and brought back under the body (Fig. 2A, frames 3–4) during the 'converge' phase.

XROMM data reveal the 3D skeletal kinematics underlying these phases (Fig. 2B,C). Overall, pelvic motion is dominated by transverse displacement (~13 cm to the right in the illustrated sequence; Fig. 2C, green). The pelvis yaws (blue) 25 deg to the left,

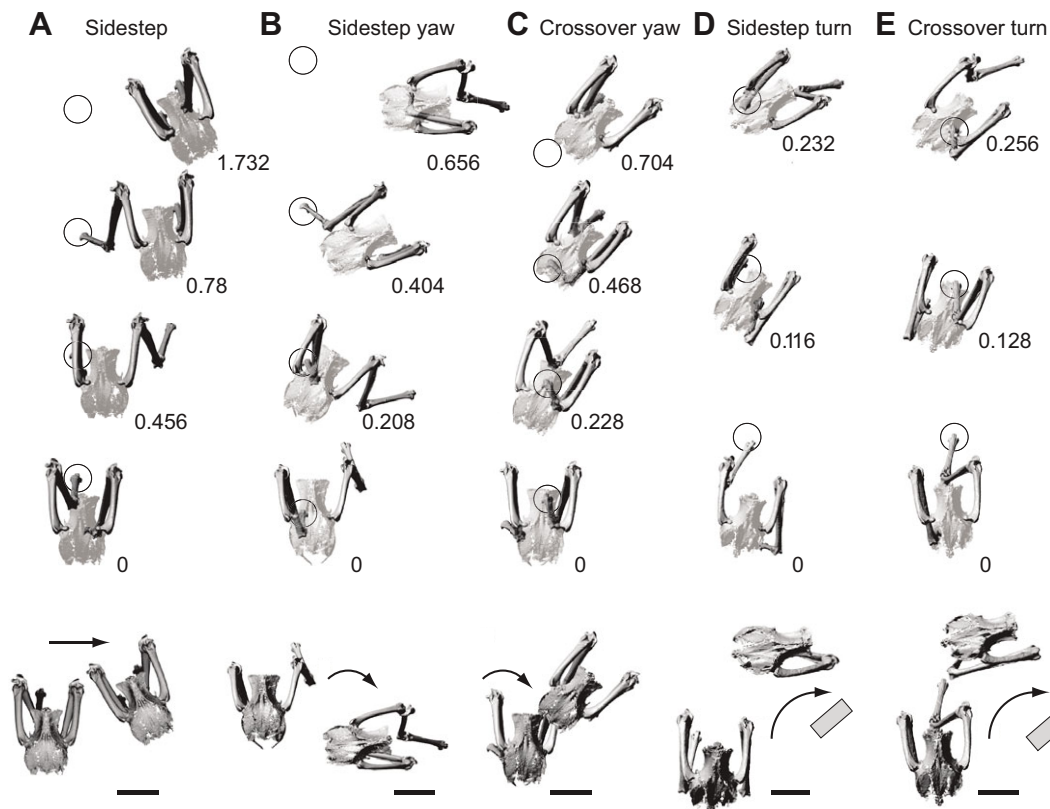


**Fig. 1. Types of maneuver in this study.** Top views of the pelvis and major hind limb bones during a sidestep (A), sidestep yaw (B), crossover yaw (C), sidestep turn (D) and crossover turn (E) reconstructed by XROMM. Numbers below the images indicate the time (in seconds) at which each pose occurred. Bottom, the starting and ending poses are shown in world space, with arrows schematically representing the major body motion. Top, pose sequences are rendered up the page with semitransparent pelvises allowing the limbs to be seen underneath. Each sequence has a fixed ground point (circle) marked under the primary stance foot as a reference. Gray boxes in D and E represent the corners of the barrier the bird negotiated. Scale bars at the bottom of each column represent 5 cm.

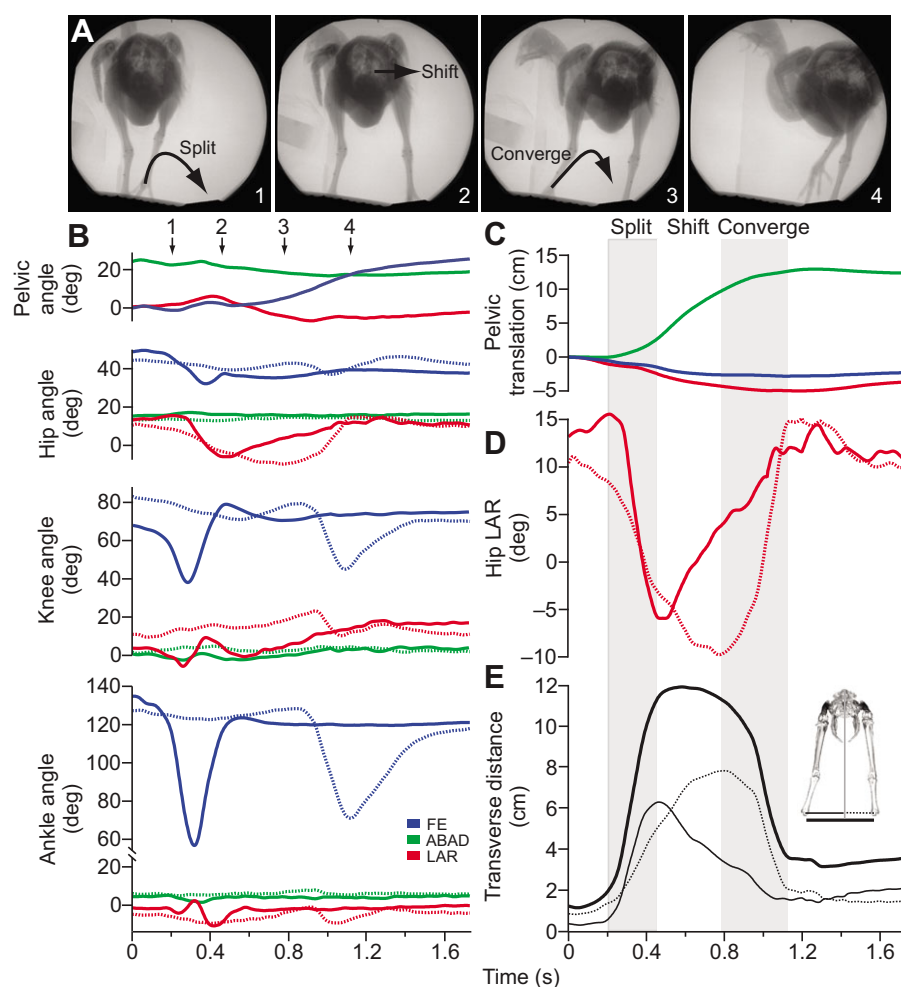


**Fig. 2. Three-dimensional hind limb kinematics of a sidestep maneuver to the right.** (A) Four frames of X-ray video showing the bird performing a split (1–2), shifting on two legs (2–3) and converging (3–4). (B) Plots of pelvic yaw (blue), pitch (green) and roll (red) as well as flexion/extension (FE, blue), abduction/adduction (ABAD, green) and long-axis rotation (LAR, red) angles of the hip, knee and ankle joints for the right (solid) and left (dotted) limbs versus time. Numbered arrows show the timing of the four X-ray frames pictured in A. (C) Pelvic translations along the craniocaudal (red), right–left (green) and vertical (blue) axes relative to the starting position. The 12.5 cm shift to the right is the dominant movement as seen in Fig. 1A. (D) LAR angles of the right (solid) and left (dotted) hips tightly correlate with transverse distance between the feet (E, inset; also see Fig. 11B). During the split phase, the right, leading foot is lifted and both femora rotate internally, spreading the feet. In double support the left hip continues to internally rotate while the right rotates externally to shift the body. During the converge phase, the left, trailing foot is lifted and bilateral external LAR brings the feet back together.

itches (green) down slightly, and rolls (red) by first raising the right hip and then the left. Angular rotations for the right (solid lines) and left (dotted lines) limbs show very little ABAD variation (green). FE excursions (blue) increase progressively from hip to knee to ankle. Right limb joints flex and then extend during the split phase, followed by a similar pattern for the left limb during the converge phase. LAR (red) occurs at all six joints, being smallest at the ankles and consistently large at the hips.

Comparison of hip LAR (Fig. 2D) with transverse distance of the feet from the pelvic median plane (Fig. 2E) reveals a coupling between femoral rotation and gross limb motion. During the split phase, both hips internally rotate (decreasing 21 and 12 deg for the right and left, respectively) as both feet move away from the midline. Pelvic translation during the shift phase is accompanied by counter-rotation of the hips; the left continues internal LAR, whereas the right changes to external LAR. During the converge phase, the hips both externally rotate and the distance between the feet decreases.

### Sidestep yaws

Birds commonly executed sidestep yaw maneuvers to face in a new direction. Based on body and footfall patterns, we identified the same three phases (split, shift and converge) in the sidestep yaw as we had found in the sidestep (Fig. 3A). However, unlike the simpler transverse displacement, the pelvis yaws significantly (80 deg to the right in the plotted sequence; see Fig. 1B) throughout all three phases. The feet not only spread and reconverge but also reorient to the bird's new heading.

Sidestep yaws exhibited hip LAR patterns quite similar to sidesteps (Fig. 3A). Femora internally rotate in the split phase, counter-rotate in the shift phase and externally rotate in the converge phase. However, sidestep yaw maneuvers are typically distinguished by the presence of substantially more knee LAR opposite that of the hip (Fig. 3A). Tibiotarsi externally rotate during the split, counter-rotate during the shift and internally rotate during the convergence. In the sequence shown, the right and left knees undergo ~55 and ~58 deg of LAR excursion, respectively. Near the end of this trial, the trailing left tarsometatarsus converges upon and then passes the right, leaving the legs crossed as shown by a negative total transverse distance.

### Crossover yaws

A second reorientation maneuver observed was the crossover yaw (Fig. 3B). In complete crossovers, three analogous phases were identified, with yaw taking place throughout (~38 deg to the right in the plotted sequence; see Fig. 1C). During the 'cross' phase, the left limb is lifted and moved medially past the right limb. As the pelvis yaws, the total transverse distance drops below zero and both feet cross the pelvic midline. In the 'shift' phase the bird transfers weight from the right foot to the left foot. Finally, in the 'uncross' phase, the right limb is lifted and moved laterally to spread the legs.

Hip LAR, knee LAR and transverse distance plots for crossover yaws (Fig. 3B) resemble mirrored versions of those for sidestep yaws (Fig. 3A). The femora externally rotate while the tibiotarsi internally rotate in the cross. During the shift the hips and knees both counter-rotate, such that each hip undergoes the same directional

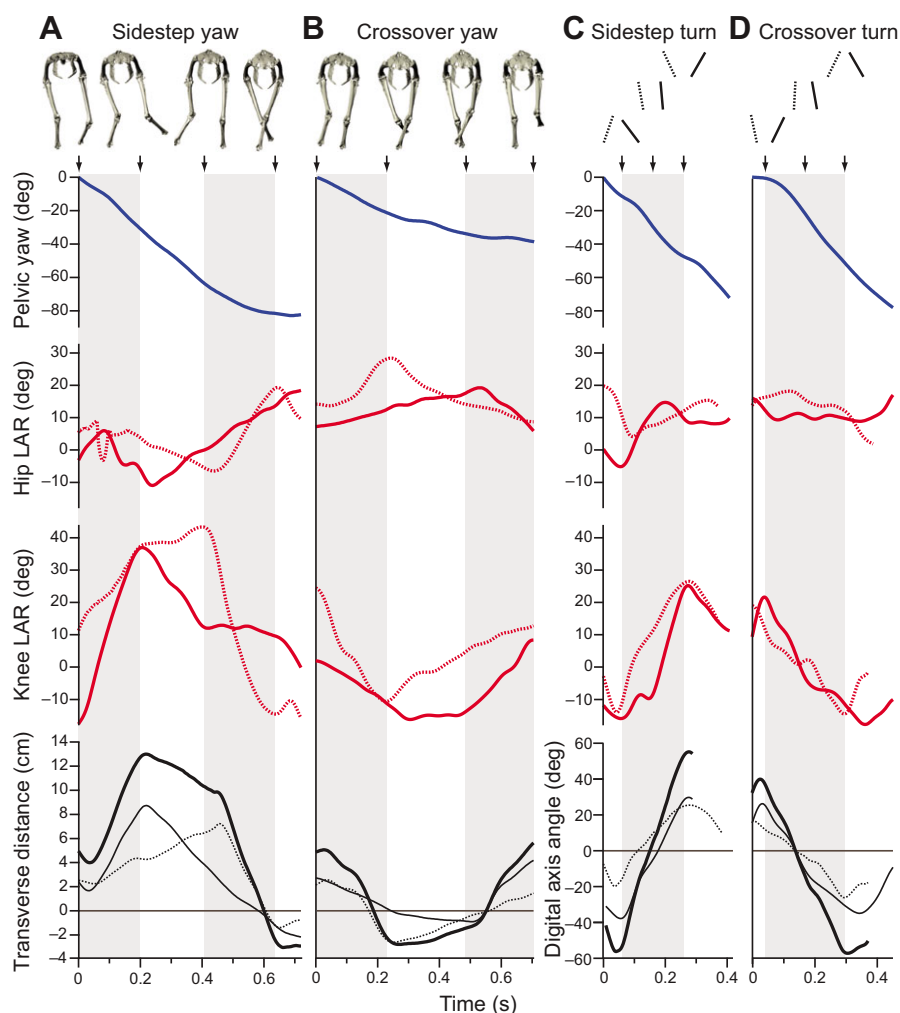


**Fig. 3. Bilateral hip and knee LAR of yaws and turns to the right.** (A) A sidestep yaw of 84 deg entails significant LAR of the femora and tibiotarsi, which counter-rotate to spread, converge and reorient the feet as in Fig. 1B. (B) Reversing the sequence of hip and knee LAR results in both feet passing the midline in a crossover yaw of 38 deg as in Fig. 1C. (C) A sidestep turn reorients the pelvis 73 deg while laterally displacing the pelvis 5 cm as in Fig. 1D. Almost 120 deg of total foot yaw is associated with external knee LAR. (D) A crossover turn with 78 deg of yaw and 5 cm of lateral displacement as in Fig. 1E is dominated by internal knee LAR. At the top of the figure, caudal views (yaw removed) of the sidestep and crossover yaws demonstrate the spreading and converging of the feet (A,B) at the four times indicated by arrows. Pairs of digital axis angles at the three time points indicated by the arrows for the sidestep and crossover turns are given in C and D (see Fig. 11B).

LAR as its contralateral knee. The uncross phase entails internal hip LAR and external knee LAR.

### Sidestep turns

Sidestep turns resemble the first, 'split' phase of a sidestep yaw superimposed on forward walking. In the sidestep turn shown in Fig. 3C, the individual yaws ~71 deg while beginning to negotiate a corner to the right (Fig. 1D). Hip LAR changes little; external LAR at both knees predominates as the digital axis angles rotate from toe in to toe out. A 'shift' phase is either unclear or relatively abbreviated. The third, 'converge' phase seamlessly transitions into the 'cross' phase of a crossover turn in the subsequent step.

### Crossover turns

Crossover turns entail the outside foot passing in front of the inside foot while moving forward. In the illustrated maneuver in Fig. 1E, the individual initiates cornering to the right and yaws ~78 deg (Fig. 3D). Knee LAR and digital axis angle plots mirror the sidestep turn data; no clear patterns of hip LAR are evident. Both knees internally rotate during the cross phase, when the digital angles change from positive to negative. A brief shift phase of counter-rotating knee LAR is followed by an 'uncross' phase that blends into the next sidestep turn maneuver.

### Complexity and variation

Rather than executing discrete maneuvers that began and ended with a neutral pose, birds often blended together a series of partial

maneuvers in succession. In the 4.2 s long sequence in Fig. 4, an overall clockwise net yaw of -252 deg entailed dramatic changes in transverse foot movements and complex LAR coordination among the hips and knees. Sidestep and crossover patterns can be distinguished, however. For instance, during the initial yaw to the left in the first highlighted section, the legs begin to spread and then the swing right limb moves medially past the stance left limb to achieve a negative transverse distance. External hip LAR is combined with internal knee LAR, matching the coordination pattern of the cross phase of the crossover yaw. In the third highlighted sequence, the bird lifts and laterally displaces its right limb while yawing to the right. Internal hip LAR and external knee LAR accompanied spreading of the feet as in the split phase of a sidestep yaw.

Each category of maneuvering, which showed comparable interlimb and intralimb coordination, was associated with consistent LAR patterns. However, birds exhibited substantial variation in the magnitudes of pelvic yaw, transverse distances, digital axis angles and LAR. Such variation precluded straightforward statistical comparison, but we present averages and ranges of LAR excursions at the hip, knee and ankle for multiple trials in Table 1. These data demonstrate the prevalence of LAR in these qualitatively similar, yet non-repetitive behaviors.

### DISCUSSION

This study presents the first six d.f. analysis of avian skeletal kinematics during terrestrial locomotion based on X-ray imaging.



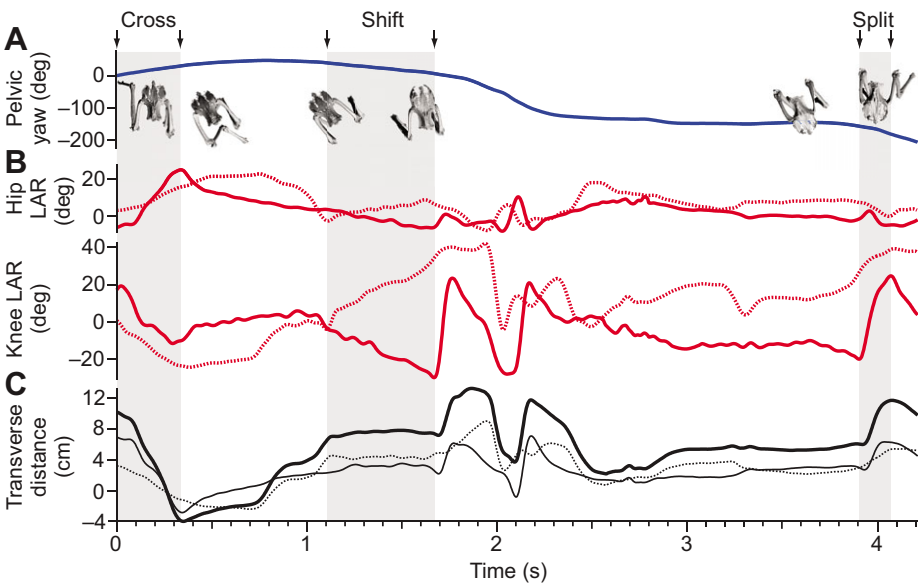


**Fig. 4. Bilateral hip and knee LAR during a complex maneuvering sequence.** (A) Plot of pelvic yaw. Overhead views show poses at the time points indicated by the arrows. (B) Plots of hip and knee LAR for right (solid) and left (dotted) limbs demonstrate that multiple maneuvers are strung together in series during the course of the trial. The left knee rotates through more than 65 deg over the sequence. (C) Transverse distances vary dramatically over the course of the maneuver as split, shift and crossover components are freely mixed. Gray boxes highlight specific coordination patterns discussed in Results.

Because guineafowl are well sized for the biplanar imaging volume, we were able to visualize, reconstruct and measure three rotations and three translations of the pelvis as well as both femora, tibiotarsi and tarsometatarsi. Sidesteps, yaws and turns reveal a previously unappreciated range and complexity of non-planar hind limb movement (Fig. 5). Guineafowl spread, cross and reorient their feet dramatically to transversely displace and turn their body. Analysis of maneuvers affords a vivid glimpse of how birds coordinate multiple d.f. within joints, among joints and among limbs to operate in 3D. These kinematic patterns provide context for interpreting the articular morphology, control mechanisms and evolutionary history of avian locomotion.

**A predominant role for LAR**

Contrary to the traditional 2D caricature of ‘erect’ bipedalism, guineafowl hind limbs clearly have the capacity to operate outside parasagittal planes during maneuvers. Rather than having hinge-like joints restricting motion to a plane (e.g. Coombs, 1978), birds

combine FE with LAR. Coordinated rotation of the femora and tibiotarsi about their long axes expands the limbs’ workspace. Guineafowl typically stand with hip heights of ca. 20 cm, yet can vary their distal tarsometatarsal spacing as much as 17 cm (–4 to 13 cm total transverse distance). Moreover, within our sample sequences, a single foot reoriented from toe in to toe out over 78 deg, while the maximum digital axis angle difference between two feet within a single trial was 112 deg (Fig. 3C).

The hip acts as a two rotational d.f. joint. ABAD excursions during maneuvers were extremely small (less than 8 deg across all six trials shown), as expected given interaction between the proximal femur and the pelvic antitrochanter (Hutchinson and Gatesy, 2000; Hertel and Campbell, 2007; Troy et al., 2009). However, contrary to the assertion that the antitrochanter prevents femoral long-axis mobility by acting as a lock (Hertel and Campbell, 2007), we document significant hip LAR in maneuvering guineafowl. For example, the sidestep in Fig. 2 entails a left hip LAR excursion of 25 deg. The bird’s ability to modulate LAR independently is demonstrated whenever two different LAR angles (such as –10 and 15 deg) are measured with FE and ABAD angles that are essentially unchanged (Fig. 6A). Thus, we find no evidence that femoral LAR is either fixed or rigidly coupled to FE as predicted by ‘cylinder-in-cylinder’ or ‘drum-in-trough’ models of antitrochanter function (Coombs, 1978; Hertel and Campbell, 2007).

Like the hip, the knee also appears to act as a two rotational d.f. joint. Similar to the human knee, the guineafowl knee is

**Table 1. Excursions of long-axis rotation (deg) for various maneuvers**

	Mean	s.d.	Min.	Max.	N
Sidestep					
Hip	18.4	6.1	10.7	25.0	6
Knee	20.6	5.7	12.9	26.2	4
Ankle	11.0	6.2	5.4	19.8	4
Sidestep yaw					
Hip	14.0	8.0	5.9	25.9	8
Knee	36.7	18.7	3.6	57.8	8
Ankle	15.8	2.8	12.9	20.4	5
Crossover yaw					
Hip	21.1	8.5	10.5	34.2	8
Knee	31.3	15.0	7.1	56.4	7
Ankle	11.0	3.2	6.9	14.7	6
Sidestep turn					
Hip	8.0	5.5	1.9	13.8	4
Knee	18.5	3.6	16.4	23.9	4
Ankle	11.6	1.1	10.8	12.3	2
Crossover turn					
Hip	6.25	5.3	1.5	11.9	4
Knee	25.6	14.0	7.2	40.2	4
Ankle	11.2	5.1	7.6	14.8	2



**Fig. 5. A sample of non-planar limb poses.** Cranial views of limbs deviating widely from parasagittal. Right and left limbs move symmetrically or asymmetrically as the situation requires. However awkward and unlikely looking, all were freely performed by the maneuvering birds.

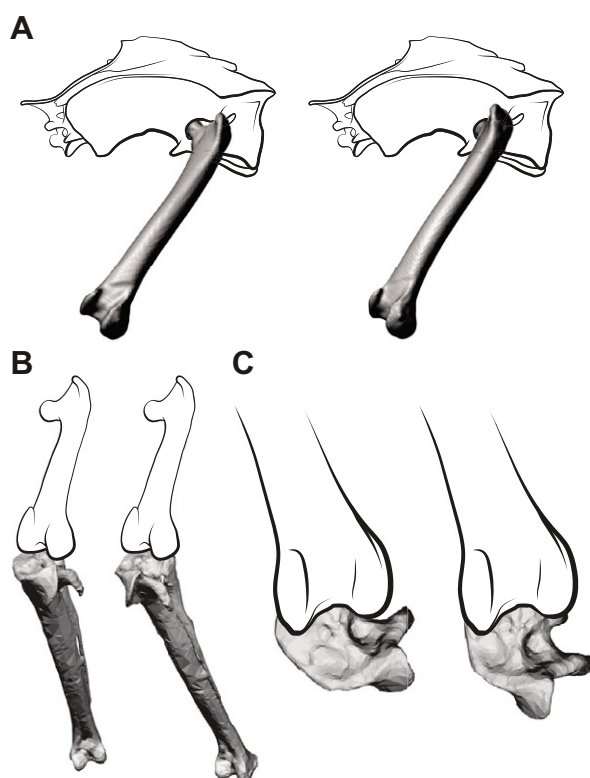


**Fig. 6. LAR at similar FE angles within the same sequence.**

(A) Craniolateral view of the left femur relative to a fixed pelvis at two different hip LAR angles ( $\sim 10$  deg,  $15$  deg) for the same FE angle ( $42$  deg). (B) Cranial view of the left tibiotarsus relative to a fixed femur at two different knee LAR angles ( $0$  deg,  $37$  deg) for the same FE angle ( $79$  deg). (C) Proximal articular view of the knee in the same poses as in B.

bicondylar and motion is constrained by medial and lateral collateral ligaments. These ligaments seem well positioned to resist disarticulation of either femoral condyle from the tibial plateau during ABAD. Large changes in FE angle are expected from a hinge-like joint, but we also measured LAR excursions of substantial magnitude. Over the course of the complex maneuver shown in Fig. 4, the left knee undergoes more than  $65$  deg of LAR. As with the hip, the knee is also able to exploit a range of LAR angles at a given FE angle. At two times within this sequence, when the left knee is flexed to  $79$  deg, LAR angles differ by  $37$  deg (Fig. 6B,C). Unlike a coupled 'screw-home' motion (e.g. Markolf et al., 1976), these data are evidence that birds actively control LAR independently of FE.

The ankle (intertarsal) joint most closely resembles a one d.f. hinge joint. Across maneuvers, changes in both LAR and ABAD were relatively small. Congruence between the tibiotarsal condyles and the tarsometatarsal cotyles, as well as ligaments and menisci, appear to permit large FE excursions while limiting other d.f.

Our data demonstrate that hip LAR and knee LAR are the fundamental d.f. underlying non-planar limb movement. Across the six trials presented (Fig. 7), the ranges of observed hip LAR angles (right  $36$  deg/left  $38$  deg) actually exceed hip FE angles ( $31$  deg/ $30$  deg). Ranges of observed knee LAR angles do not exceed knee FE angles ( $79$  deg/ $80$  deg), but they are substantial ( $67$  deg/ $68$  deg). These summary data are not dominated by a single individual or maneuver. Within single trials, LAR angle ranges sometimes rival or exceed FE ranges at the hips and knees.

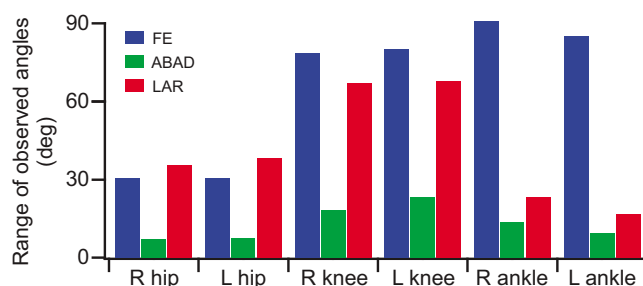


**Fig. 7. Ranges of observed joint angles.** For each joint, the difference between the maximum and minimum values of FE, ABAD and LAR angle were calculated across the six trials figured in this paper. L, left; R, right.

### LAR: consequences and coordination

The kinematic impact of hip and knee LAR is most easily understood by considering limb movement relative to a fixed pelvis. We first address the hips. Because the femur is held sub-horizontally and the knee is relatively flexed, the distal tarsometatarsus and toes lie far below the femoral long-axis. Therefore, hip LAR primarily moves the distal limb transversely (Fig. 8B) (Hutchinson and Gatesy, 2000). Internal LAR spins the cranial surface of the femur medially, which sends the ankle and toes laterally (increasing transverse distance from the pelvic midline). External LAR produces the opposite result, bringing the limb medially and decreasing transverse distance. Small changes in hip LAR engender comparatively large distal displacements.

When both hips internally rotate, the legs spread. Birds typically employ bilateral internal LAR with one foot on the ground and one in swing. Such coordination is evident during the split phase of sidesteps and sidestep yaws, and during the uncross phase of crossover yaws. Bilateral external LAR characterizes the converge phase of sidesteps and sidestep yaws, as well as the cross phase of crossover yaws. When birds counter-rotate their femora, the two feet move in the same direction. Combinations of external and internal hip LAR are found in the shift phase, when the body translates laterally over two planted feet.

At the knee, LAR has two effects on the distal limb. Because the ankle is typically flexed, knee LAR moves the distal tarsometatarsus transversely and reorients the foot (Fig. 8C). Internal knee LAR spins the cranial surface of the tibiotarsus medially, sending the foot medially and directing the toes inward (decreasing the digital axis angle). External knee LAR produces the opposite result, increasing transverse distance and digital axis angle.

When both knees externally rotate, the feet spread and toe out. Birds use bilateral external LAR during the split phase of sidestep yaws and sidestep turns, as well as during the uncross phase of crossover yaws. Synchronous internal knee LAR characterizes the converge phase of sidestep yaws and the cross phase of crossover yaws and turns. During the shift phase of sidestep and crossover yaws, and during the shift phase in the complex maneuver sequence (Fig. 4), the knees can break symmetry as the bird transitions from one stance foot to the other. This knee counter-rotation is used to shift weight from one limb to the other.

Many of the trials presented here demonstrate that hip and knee LAR are coordinated during maneuvers. Often, rotations are complementary within each limb (Fig. 8D). For instance, during sidesteps and sidestep yaws, internal LAR at the hip is often accompanied by external LAR at the knee (Fig. 2B, Fig. 3A). Internal hip rotation moves the foot laterally and external knee rotation drives the foot laterally farther still. During crossover yaws,

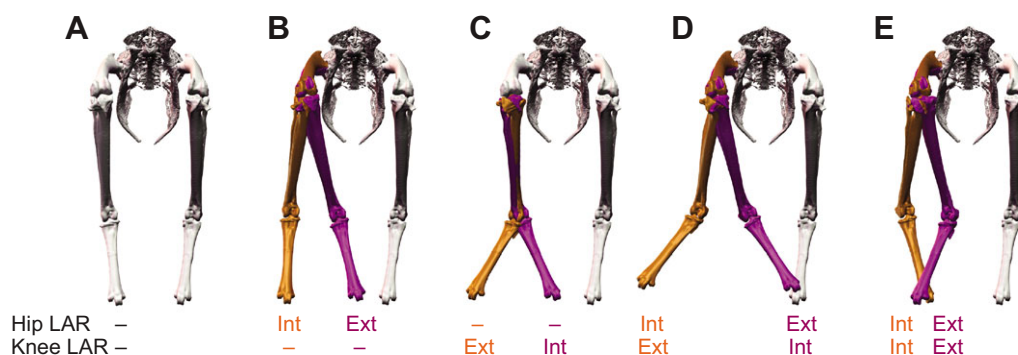


**Fig. 8. Individual and combined consequences of LAR.** (A) Cranial view of a neutral pose. (B) Internal hip LAR (orange) moves the right foot laterally while external hip LAR (purple) moves the foot medially. (C) External knee LAR (orange) moves the right foot laterally and toes out while internal knee LAR (purple) moves the foot medially and toes in. (D) Internal hip LAR and external knee LAR (orange) are additive, as are external hip LAR and internal knee LAR (purple). (E) Combining internal (orange) and external (purple) LARs generates a range of digital axis angles at a similar toe position.

rotation patterns are typically reversed (Fig. 3B). External hip rotation and internal knee rotation additively bring the foot medially under the body.

These are not the only coordination patterns we observed. The shift phase in Fig. 4 shows LAR at the hips and knees apparently conflicting, presumably to maintain pelvic roll during the maneuver. The knee and hip also both externally rotate early in the sidestep turn and at the end of the crossover turn (Fig. 3C,D). Such examples highlight how the animal can mix and match LAR at the hip and knee to accomplish different tasks, from sidestepping, to reorienting the body, to navigating around obstacles (Fig. 5). It is not always possible to isolate specific behaviors within a sequence, as the subject smoothly blends maneuver elements together to accomplish its goals (Fig. 4). Short periods of coordination can be identified, but often transition into complex combinations of rotations that are difficult to interpret. The differences between yaws and turns also reflect an ability to combine motions. Knee LAR patterns remain similar between yaws and turns, but the addition of forward motion makes hip LAR patterns less clear.

### Comparison with previous 3D kinematic analyses

Other 3D studies of avian bipedal locomotion differ methodologically from our guineafowl work in important ways. Most X-ray and standard imaging analyses track only one skin marker or skeletal landmark per joint (Jindrich et al., 2007; Abourachid et al., 2011; Hugel et al., 2011; Nyakatura et al., 2012; Provini et al., 2012; Andrada et al., 2013a; Andrada et al., 2013b). 3D joint coordinates can be linked into a stick figure, but LAR cannot be directly measured from such line segment models (Gatesy et al., 2010). Kinematic redundancy leaves the precise interplay among d.f. responsible for limb movement ambiguous. Hip LAR can be mistaken for knee ABAD and knee LAR can be confused with ankle ABAD (Fig. 8), yet these motions have profoundly different implications internally for both soft and hard tissues.

Using clusters of topical markers provides not only superior 3D tracking over single points but also six d.f. measurement of kinematics (Rubenson et al., 2007; Rubenson et al., 2011; Goetz et al., 2008). However, for proximal segments, even this technique likely suffers from so-called ‘errors of transformation’ (Zatsiorsky, 1998). LAR is particularly sensitive to skin motion artefacts (Cappozzo et al., 1996; Reinschmidt et al., 1997), and so remains the most difficult rotational d.f. to measure accurately. As described by Rubenson and colleagues: ‘...hip internal/external rotation exhibited large variability between the animals and between separate trials of the same animal, possibly

reflecting limitations in the measurement techniques. The calculation of long-axis femur rotation assumed that the external femur marker cluster represented the underlying limb movement. Because the markers cannot easily be secured around the thigh segment on ostriches, some long-axis rotation may occur underneath the marker cluster. More accurate calculation of femoral rotation in this species may require cineradiography techniques...’ [see p. 2558 of Rubenson et al. (Rubenson et al., 2007)]. Indeed, the marker-based XROMM approach reconstructs bone position and orientation without the soft tissue artefacts and marker occlusion problems inherent in optical motion capture.

The ostrich study of Rubenson and colleagues (Rubenson et al., 2007) also differed from the present study in the construction of joint coordinate systems (JCSs). Rather than only using skeletal anatomy to define anatomical coordinate systems (ACSSs) as done here, the orientation of each FE axis was calculated as the mean helical axis from dynamic tests of a cadaver limb (Besier et al., 2003). Much of the non-planar motion in running could be explained by FE about these axes, which were neither parallel nor transversely oriented as assumed in 2D analyses (Rubenson et al., 2007; Hugel et al., 2011). However, significant ABAD and LAR were reported, demonstrating that rotation at the knee cannot be reduced to a single dimension.

Although we agree that such ‘functional’ axes may minimize ‘kinematic cross-talk’ between rotational d.f. (Piazza and Cavanagh, 2000), we believe anatomical definitions of coordinate systems (Appendix) are useful for a number of reasons when considering high-resolution skeletal motion, such as XROMM-derived datasets. First, we are interested in the evolution of limb morphology and function through time. Purely anatomical axes provide a means to compare joints and movement across all taxa, both living and extinct. Second, our ACSSs and JCSs (particularly rotation order) reflect hypotheses of motion based on simple geometric models. For example, the cylindrical contours of the femoral condyles are expected to strongly influence joint excursions during forward movement. Finally, the use of only skeletal morphology to build ACSSs may facilitate the identification of soft tissue contributions to joint function.

Even when ACSSs and JCSs are based on bony anatomy, different choices of axes and rotation order will generate different kinematic data for the same movement. We designated LAR axes that run along the proximo-distal length of each bone. By this convention, pure LAR spins each segment in place with minimal displacement of its distal condyles, thereby portraying segment kinematics most clearly. Alternatively, one might choose axes that most accurately



depict the interaction among articular surfaces comprising a joint. To describe human knee kinematics, for example, the LAR axis is sometimes oriented normal to the tibial plateau (Miranda et al., 2010; Scanlan et al., 2012; Kaiser et al., 2013). This standard allows the femoral condyles to remain articulated during LAR.

We measured surprisingly large ABAD excursions at the knee (ca. 16 deg in the sequence shown in Fig. 4), but do not believe that the femoral condyles actually disarticulate from the tibia and fibula. Rather, ABAD rotations reflect a tibial plateau that is tilted by ca. 20 deg relative to our LAR axis (Fig. A1D). If we reorient the LAR axis of the proximal tibiotarsal ACS normal to the plateau, we can reduce ABAD excursion to less than half the measured value, but then measure FE angles that are 20 deg larger than the observed angle between segments. Thus, there is no single JCS that satisfies the goals of segment-based and joint-based knee kinematics simultaneously. All suffer from some form of 'kinematic cross-talk' (Piazza and Cavanagh, 2000; Rubenson et al., 2007), yet the reality of the enormous LAR excursions we document (e.g. Fig. 6) cannot be dismissed as artefact.

### Evolution of LAR in birds and other theropods

Our results raise many new questions about the evolution of birds, as well as the history of bipedality in dinosaurs. How representative are guineafowl? Given the prominence of LAR during maneuvering steps, has the extent of LAR been underappreciated during straight running as well? Do all extant birds employ large amounts of hip and knee LAR, making this mechanism of limb control primitive for Neornithes? If so, is substantial LAR a primitive feature of theropods, or did it co-evolve later with small body size, tail reduction (Gatesy, 1990), pectoral enlargement (Allen et al., 2013), flight, perching ability, or some other trait? Can osteological correlates of LAR be identified in modern skeletons and in the fossil record? Many researchers infer a more extended limb pose in non-avian theropods (Gatesy, 1990; Hutchinson and Gatesy, 2000; Hutchinson and Allen, 2009), with a more vertically oriented femur and a more extended knee. If so, hip LAR would be relatively ineffective for controlling transverse foot placement compared with hip ABAD. However, both hip and knee LAR would modulate digital axis angle.

### Conclusions

Although the importance of LAR and torsional loading is well accepted in so-called 'sprawling' forms (Brinkman, 1981; Jayne and Irschick, 1999; Blob and Biewener, 2001; Reilly et al., 2005), non-sagittal motion is often overlooked when considering more upright taxa (but see Carrano, 1998; Hutchinson and Gatesy, 2000; Gosnell et al., 2011). Limiting research to a 2D perspective risks oversimplifying the problem in ways that yield unrealistic hypotheses and interpretations. Similarly, restricting analyses to steady walking or running yields an incomplete sampling of joint mobility. The critical role of LAR in maneuvering reveals that the passive and active mechanisms responsible for coordinating rotational d.f. are important even when LAR excursions are reduced. For both evolutionary and robotic (e.g. Hugel et al., 2011) questions, a more complete understanding of the avian hind limb biomechanics requires integrated 3D analysis of morphology, kinematics and kinetics across a range of locomotor behaviors.

### MATERIALS AND METHODS

#### Individuals, marker fabrication and surgical implantation

Five adult ( $1.41 \pm 0.20$  kg) helmeted guineafowl (*N. meleagris*) were obtained from a local breeder for use in this study. Animals were housed in the Animal Care Facility at Brown University with unlimited access to food and

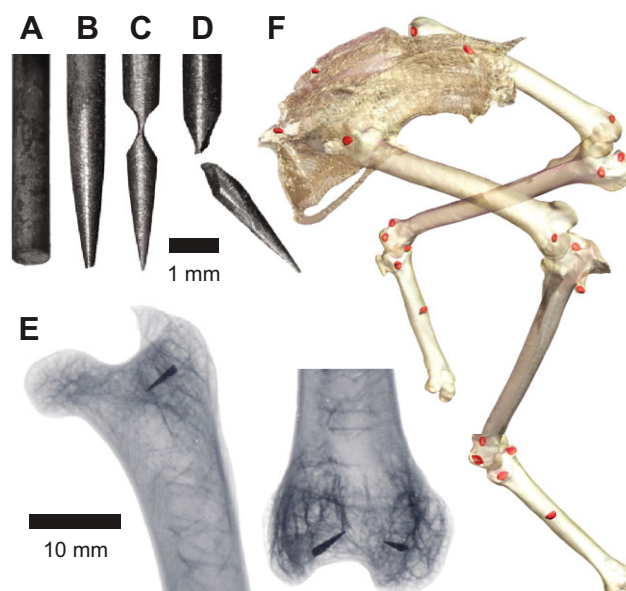


**Fig. 9. Marker-based XROMM using carbide points.** (A–C) Three steps in the fabrication of a conical marker from a stock rod. (D) The thinned blade is strong enough to allow manual insertion, but weak enough for the tip to snap off when bent. (E) Planar X-ray of points implanted into the proximal and distal femur. (F) Implant sites shown by polygonal marker models (red) within their respective bone models.

water. All surgical and experimental techniques were approved by Brown University's Institutional Animal Care and Use Committee.

Marker-based XROMM entails implantation of three or more metal markers into a bone to provide 3D coordinate data for calculating its rigid body transformations (Brainerd et al., 2010). For most applications, small metal spheres (typically tantalum) are inserted into pre-drilled holes (Dawson et al., 2011; Gidmark et al., 2013; Nowroozi and Brainerd, 2013). In guineafowl, the thin cortices and foam-like trabeculae of the pelvis and long bone epiphyses are not amenable to bead implantation. Moreover, surgical access to bone surfaces for drilling and bead insertion is limited in some areas. We therefore opted to implant conical carbide steel points as first described for marking starling bones (Jenkins et al., 1988; Dial et al., 1991).

Conical markers were individually fabricated (Fig. 9A–C) by hand-grinding cylindrical carbide rods (0.8 mm diameter unground premium carbide, RR2, California Tool and Engineering Inc., Riverside, CA, USA). First, the tip of each rod was roughly shaped into a point using a silicon carbide grinding wheel (Norton no. 75942391, 8 in diameter, 120 grit, MSC Industrial Supply Co., Melville, NY, USA) and cleaned with steel wool. Rough points were then sharpened under a dissecting microscope using a Dremel hand drill (Dremel Stylus Model no. 1100, Dremel, Mt Prospect, IL, USA) equipped with a diamond burr (10 mm diameter, 3 mm long, 400 grit, BSW4, Lasco Diamond Products, Chatsworth, CA, USA). The angled rims of the diamond burr were used to incise two grooves, leaving a blade-like stem attaching the ~2.5 mm long point to the remainder of the rod. After preparing both ends, rods were autoclaved with the rest of the surgical kit.

Birds were sedated with Butorphanol; anesthesia was induced and maintained with isoflurane. Carprofen and enrofloxacin were administered as an analgesic and antibiotic, respectively. Marker points were inserted using sterile pin vises. The tip was manually forced into the target bone and then broken off at the weak zone (Fig. 9D,E). By not requiring pre-drilling, the 'Jenkins technique' allows us to implant difficult to reach sites via very small incisions and, if necessary, through overlying muscle. To mark the tarsometatarsus and distal tibiotarsus we make no incisions at all and simply pierce directly through the skin between scales. For particularly porous sites like the posterior ilium, we create especially thin blades so that points can be snapped off without damaging the delicate bone.

Three markers were inserted into the pelvis: a single anterior midline marker at the dorsal tip of the crista spinosa synsacri, and two markers in



the postacetabular wings of the ilium laterally. Three markers were placed into the femur: a proximal marker in the lateral surface of the trochanter, and distal markers in the lateral and medial condyles (Fig. 9E). Four markers were implanted into the tibiotarsus: a proximal marker in the lateral cnemial crest, a proximal marker in the medial aspect of the tibial plateau, and two distal markers in the medial and lateral epicondylar depressions. Three markers were inserted into the tarsometatarsus: two proximal markers in the dorsal ridge of the cotyla, and one dorsolateral marker mid-shaft. All individuals recovered quickly, typically walking normally within an hour of skin closure, and showed no obvious gait abnormalities.

Seven bones (pelvis and both legs) were surgically implanted in three individuals (Fig. 9F). Of the remaining two, one was implanted unilaterally (four bones) while the other was implanted unilaterally with bilateral femoral implants (five bones).

### Data collection

Recording was performed in the W. M. Keck Foundation XROMM Facility, a custom-built biplanar X-ray room at Brown University. Each system consists of an EMD Technologies model EPS 45-80 X-ray generator, a Varian model G-1086 X-ray tube suspended from the ceiling on a telescoping crane, a Dunlee model TH9447QXH590 image intensifier (40.64 cm diameter) mounted on a mobile-arm base, and a Phantom v10 high-speed digital video camera (Vision Research, Wayne, NJ, USA) recording at 1760×1760 pixel resolution. The two X-ray beams (70–75 kV and 100 mA) were set at source to image distances of 138 cm and oriented horizontally at 90 deg, intersecting to form a volume just above the substrate (Fig. 10A). An overall resolution of  $\sim 2.3$  line pairs  $\text{mm}^{-1}$  was achieved by this imaging chain. Two additional Phantom v9.1 cameras captured a medium shot of the whole bird and a close-up shot of foot movement with standard light video (1600×1200 pixels). All four cameras recorded at 250 frames  $\text{s}^{-1}$  with 1/2000 s shutter speeds and were synchronized to within  $\pm 4$   $\mu\text{s}$ .

Maneuvering trials with minimal forward progression (sidesteps and yaws) took place within a chamber (34 cm wide×70 cm long×50 cm tall) with a floor covered in a textured plastic mat and two walls of transparent Plexiglas. For turning trials, a trackway was constructed with a  $\sim 140$  deg bend at the intersection of the X-ray beams and a darkened pet crate at each end. Birds were motivated to perform sharp, low speed turns in both directions using either an outer (sidestep) or inner (crossover) stance limb. After *in vivo* data collection was completed, subjects were induced with 5% isoflurane and killed with Beuthanasia.

### XROMM animation

A CT scan of each frozen, disarticulated specimen was made with a hospital scanner (Philips Medical System, Best, The Netherlands), which generated

512×512 pixel images at 0.625 mm intervals, with the exception of one individual that was scanned with a Fidex micro-CT scanner (Animage, LLC, Pleasanton, CA, USA) at 512×512 pixels and 0.456 mm intervals. OsiriX software (v.4.1.2, Geneva, Switzerland) (Rosset et al., 2006) was used to segment individual bones and marker clusters and to make polygonal models (decimate-resolution: 1.0, smooth-iterations: 50 except for pelvis, 1). Threshold pixel values varied widely: limb bones (400), pelvis (150), femur and tibiotarsal markers (3000), tarsometatarsal markers (3050), pelvic markers (2000). Marker density produced artefacts near the ends of limb bone models, which were cleaned in Geomagic Studio 2013 (3D Systems, Morrisville, NC, USA) primarily by deleting vertices representing artefacts and reconstructing missing bone surface with the hole-filling algorithms. Bone and marker files (.obj format) were imported into the 3D animation software (Maya 2010, Autodesk Inc., San Rafael, CA, USA). The centroid of each marker model in CT space was calculated as the average coordinates of its vertices and exported from Maya.

Rigid body kinematics were derived from biplanar X-ray videos using the XrayProject workflow for marker-based XROMM (Brainerd et al., 2010) (xromm.org), a freely available set of MATLAB (MathWorks, Natick, MA, USA) and Maya scripts that we describe here briefly. First, X-ray hardware and video camera distortion was corrected based on images of a standardized metal grid. Second, the focal spot location and beam orientation of each X-ray system were calculated by direct linear transformation using an acrylic calibration cube bearing 64 steel beads. Images of the same cube were used to calibrate one standard camera; a smaller, metal cube bearing beads was needed for the close-up standard camera. Third, the 2D coordinates of each bone marker were digitized in the two X-ray videos and combined with DLT data to reconstruct 3D marker coordinates. The autotracking and centroid-finding features in XrayProject were used when adequate marker contrast and minimal proximity allowed; all others were tracked manually. XYZ coordinates were individually Butterworth filtered at a threshold of 15 Hz to reduce high-frequency noise.

We evaluated the precision of this point tracking method by measuring the standard deviation of the distance between two markers within the same bone (Tashman and Anderst, 2003; Brainerd et al., 2010). Standard deviations of inter-marker distances were collated for 14–20 pairs per trial over 2597 frames representing the three bilaterally implanted individuals. The mean standard deviation for 99 pairwise intermarker distances resulted in an overall precision of  $\pm 0.160$  mm.

Finally, singular value decomposition was used to calculate a 4×4 transformation matrix for the marker cluster of each bone at each frame by combining digitized XYZ data with marker centroid data. Motion was reconstructed using Maya software by importing the transformation matrices to independently animate each bone model. Using DLT calibration data and Maya scripts (xromm.org), virtual cameras were positioned and aimed at

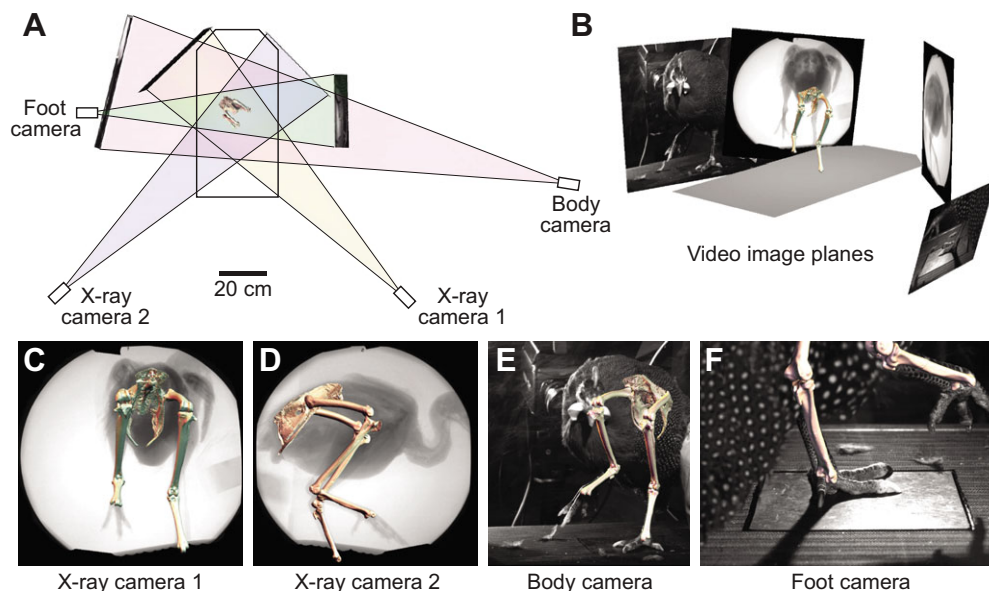


**Fig. 10. Experimental setup reconstructed as a Maya scene.**

(A) Top view of the maneuvering chamber representing the two X-ray systems as a pair of virtual X-ray cameras with overlapping yellow and blue beams. Two calibrated standard cameras (red and green fields of view) provide external imaging of the whole bird and feet. (B) Perspective view of the scene showing the reconstructed skeletal model in place between the four image planes textured with frames of video. (C–F) When viewed through each virtual camera, bone models are registered to their X-ray shadows as well as to the standard video images.

image planes, which displayed sequences of undistorted video frames as animated textures (Fig. 10). Cameras representing the X-ray beams gave the user perspectives as if viewing the scene with X-ray vision, such that a bone's or marker's correctly animated model remained registered with its image in both windows (Fig. 10C,D; supplementary material Movie 2). In two sequences, we used two-marker roscoping (Gatesy et al., 2010) to align three bone models for short series of frames (less than 10% of each sequence) in which one marker was only visible in one video.

Surgical implantation of the medial femoral condyle proved particularly difficult, leaving three individuals with only two femoral markers (trochanter and lateral condyle) per bone rather than three. For such birds we generated 'virtual' markers in the femoral heads. Based on measurements of fully marked femora ( $N=3$ ), we determined that the centroid of the femoral head remains very stable relative to the centroid of the acetabulum. Therefore, a properly animated pelvis allows the location of the femoral head to be predicted to within 0.5 mm. By animating the pelvis first, the coordinates of each acetabular centroid were exported and served as 'virtual' markers to complete the femoral triad for matrix calculations. Comparison of femoral motion reconstructed from three implanted markers with femoral motion animated from two implanted and one 'virtual' marker showed less than 0.5 deg offsets for FE and ABAD, and 2–4 deg offsets for LAR.

All calibration images, raw videos and CT files were up-loaded to the XMA Portal, a web-based environment for storage, management and sharing of XROMM data (xmaportal.org). These data will be made public upon publication.

### ACSs and JCSs

The relative motion of two bones can be measured by a JCS (Grood and Suntay, 1983) composed of two segment-fixed axes and a third, mutually orthogonal axis that 'floats' (Fig. 11A). We developed JCSs to quantify six d.f. motion of the hips, knees and ankles, as well as of the pelvis relative to

a global coordinate system. JCS axes were based on ACSs derived from fitting of geometric primitives, skeletal landmarks and inertial calculations of bone models. We provide a brief summary here; details are given in the Appendix. Rotations were described using Euler angles following a Z–Y–X rotation order, which was equivalent to the default X–Y–Z rotation order in Maya. Graphs of Z-axis rotations (yaw and FE) are shown in blue, Y-axis rotations (pitch and ABAD) in green, and X-axis rotations (roll and LAR) in red.

The Z-axes remained fixed to the proximal segment of each pair: a global vertical axis for pelvic yaw, transverse axes through the centroids of fitted acetabular spheres for hip FE, axes through fitted femoral condyle cylinders for knee FE, and axes through fitted tibiotarsal condyle cylinders for ankle FE. Yaw to the left and joint extension were positive. The X-axes remained fixed to the distal segment of each pair: a longitudinal sacral axis for pelvic roll, axes passing from the centroids of fitted femoral head spheres through the centroids of fitted femoral condyle cylinders for femoral LAR, and the least inertial axes (Crisco and McGovern, 1997) of tibiotarsal and tarsometatarsal models for knee and ankle LAR. Rolling to the left and external LAR were positive. The Y-axes 'float' to remain orthogonal to both the X- and Z-axes for each JCS: pelvic pitch and hip, knee and ankle ABAD. Head up pitching, hip abduction, knee adduction and ankle abduction were positive (note the direction switch at the knee).

To further characterize non-planar motion we also quantified foot displacement and orientation relative to the pelvic midline (Fig. 11B). We calculated the transverse distances of the tarsometatarsal condyles of digit III to the median sagittal plane. Lateral positions were deemed positive for each limb. The sum of both transverse distances measured the spread (positive) or crossing (negative) of the feet relative to the moving pelvis. We also calculated a parameter deemed the 'digital axis angle' to quantify the degree of toeing out and toeing in. Because phalangeal motion was not reconstructed in this study, we created a virtual, forward pointing digit at the intersection of the tarsometatarsal X–Y plane with horizontal. Positive angle values for each foot signified virtual digits aiming away from the pelvic midline. The sum of both angles was 0 deg when the digital axes were parallel, positive when diverging and negative when converging.

## APPENDIX

### ACS and JCS conventions

We sought to establish a set of coordinate systems for the guineafowl hind limb (Figs A1, A2) that would allow us to compare 3D motion derived from XROMM analysis among individuals and among different avian species. XROMM data presented in a common format will improve communication and be of greater utility for studying locomotor function and evolution [as in human ISB standards (Wu et al., 2002; Wu et al., 2005)]. By basing our conventions purely on skeletal anatomy, as opposed to *in vivo* or *ex vivo* motion, our scheme should be applicable to fossil birds and other extinct theropods as well. Here, we describe the criteria for determining each ACS and how pairs of ACSs were combined to form JCSs.

In order for all ACSs to be right-handed and yield JCS rotations of the same sign for comparable motion (e.g. extension positive for both knees), limb ACSs were created asymmetrically (contra Wu and Cavanagh, 1995). Each JCS drew its Z-axis from the proximal ACS, its X-axis from the distal ACS, and its Y-axis floated to remain orthogonal to both (e.g. Grood and Suntay, 1983). All JCSs thus represented 3D rotations as Euler angles using a Z–Y–X rotation order, which corresponded to the default X–Y–Z rotation order in Maya.

### Pelvic ACSs

Polygons forming the wall of each acetabulum in the pelvis model were isolated and fitted with spheres in Geomagic. To establish a pelvic ACS, an origin was created midway between sphere centroids (Fig. A1A). The Y-axis ran through the right and left acetabular

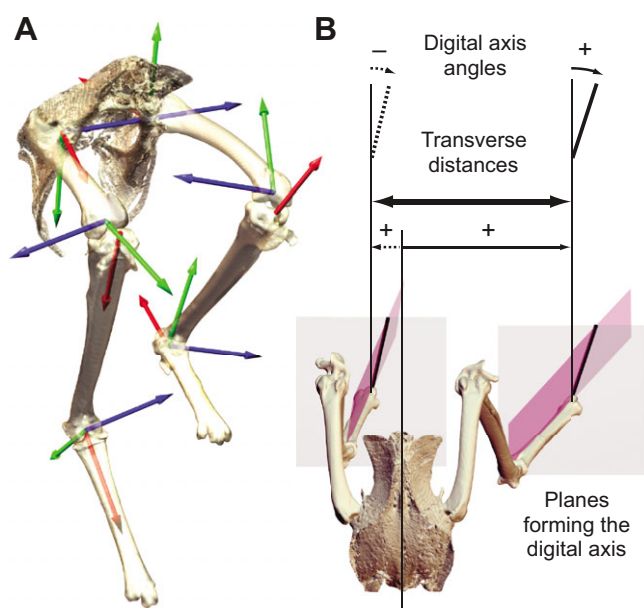


**Fig. 11. Quantifying 3D skeletal motion.** (A) Semi-transparent anterolateral view of the pelvis and hind limbs showing the anatomical coordinate system (ACS)-based joint coordinate systems (JCSs) by which FE (blue axes), ABAD (green axes) and LAR (red axes) rotations were measured at the hips, knees and ankles. (B) Top view showing how the position and orientation of the tarsometatarsus were measured relative to a median sagittal plane (thin vertical line bisecting the pelvis). Transverse distances for each foot (positive laterally) were summed to measure spreading of the feet (thick double-headed arrow). Virtual digital axes extending forward from the condyle of digit III were calculated at the intersection of each tarsometatarsal sagittal plane (magenta) with horizontal (light gray). Digital axis angle measured the toe out (positive) or toe in (negative) deviation of each digital axis from a sagittal plane.

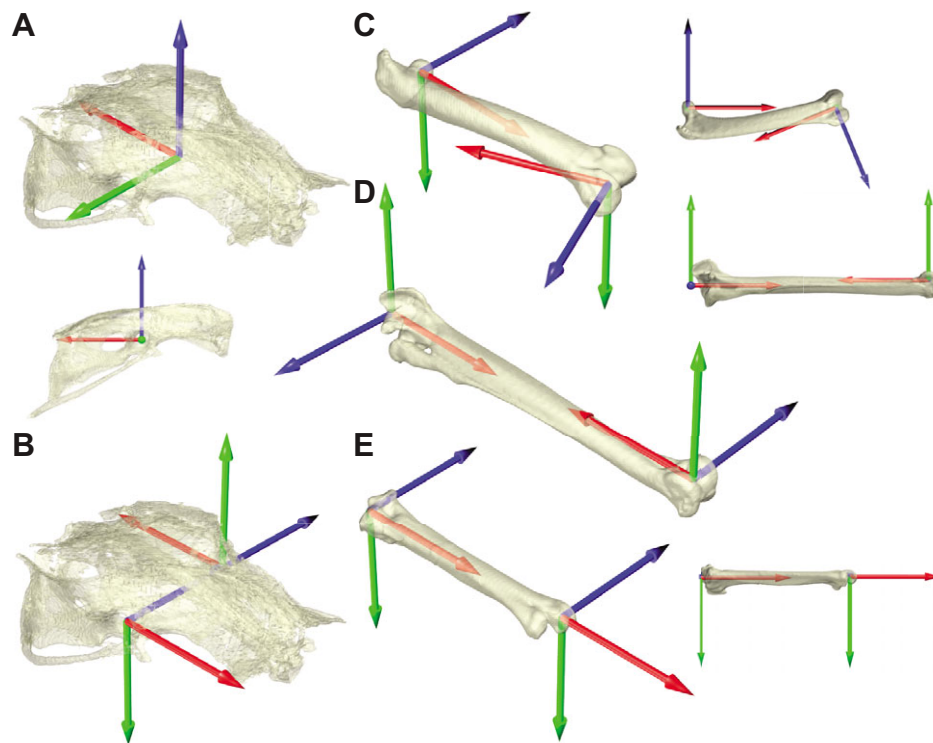


**Fig. A1. ACS conventions for each bone.**

(A) Craniolateral and lateral views of the pelvic ACS. (B) Craniolateral view of the pelvis showing acetabular ACSs for the right and left hip. (C) Craniolateral and dorsal views of the right femur demonstrating the proximal and distal femoral ACSs. (D) Craniolateral and lateral views of the right tibiotarsus showing the proximal and distal ACSs. (E) Craniolateral and lateral views of the right tarsometatarsus with proximal and distal ACSs.

centers, positive to the right. The *X*-axis ran orthogonally down the midline, intersecting the first and last sacral vertebral centra, positive pointing caudally. The *Z*-axis was set orthogonal to both *Y*- and *X*-axes, positive dorsally. Two additional ACSs, each located at an acetabular centroid, were created to measure hip movement (Fig. A1B). For both right and left acetabular ACSs, the *Z*-axes ran

transversely (both sides positive to the left), the *Y*-axes dorso-ventrally (right positive ventrally, left positive dorsally), and the *X*-axes longitudinally (right positive cranially, left positive caudally) relative to the pelvic ACS.

#### Femoral ACSs

Two ACSs were made for each femur, proximal and distal (Fig. A1C). Using Geomagic, polygons of the femoral heads were isolated and fitted with spheres, the centroids of which formed the origins of the proximal ACSs. Distally, polygons forming the two femoral condyles (not including the tibiofibular crest) were isolated and fitted with cylinders, following a method used in human biomechanics (e.g. Miranda et al., 2010). Each cylinder's centroid formed the origin of a distal ACS. Proximal *X*-axes represented femoral long axes by passing through both ACS origins (right positive distally, left positive proximally). Each cylinder's axis designated the *Z*-axis of a distal ACS (both sides positive to the right). Proximal and distal *Y*-axis vectors (right positive caudally, left positive cranially) were calculated by crossing the proximal *X*-axis with the distal *Z*-axis. Crossing the distal *Y*- and *Z*-axes yielded the distal *X*-axes (right positive proximally, left positive distally). Proximal *Z*-axes (both sides positive to the left) were calculated by crossing the proximal *X*- and *Y*-axes. Similarly, the distal *X*-axes (right positive proximally, left positive distally) were calculated by crossing the distal *Y*- and *Z*-axes.

#### Tibiotarsal ACSs

Each tibiotarsus also had a proximal and distal ACS (Fig. A1D). As with the femur, polygons forming the two tibial condyles were fitted with cylinders in Geomagic. Cylinder centroids and axes designated the origins and *Z*-axes (both sides positive to the left) of the distal ACSs. To establish bone long axes, we calculated the inertias of the tibiotarsal/fibula models by treating them as homogeneous solids (Crisco and McGovern, 1997) in MATLAB. The axes of least inertia became the proximal *X*-axes (right positive distally, left positive

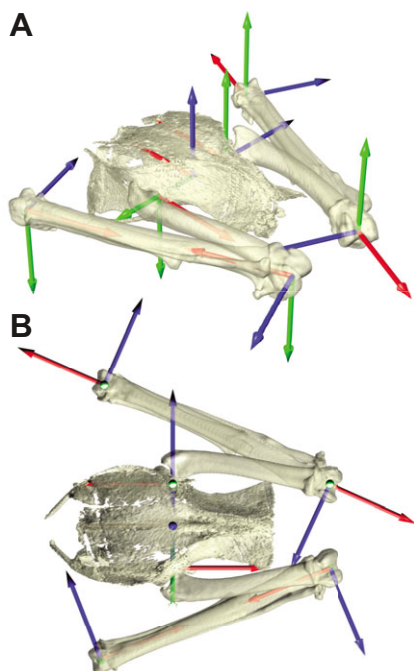


**Fig. A2. The reference pose.** (A) Craniolateral view of the reference pose, showing the JCS axes when all translations and rotations are 0. (B) Dorsal view of the reference pose. Note the right-left JCS asymmetry that allows homologous movements to have the same sign (e.g. external knee LAR both positive).



proximally), with the origins of the proximal ACSs at the level of the furthest proximal extensions of the cnemial crests. *Y*-axes for both ACSs (right positive cranially, left positive caudally) were vectors created by crossing the proximal *X*- and distal *Z*-axes. Proximal *Z*-axes (both positive to the right) resulted from crossing the proximal *X*- and *Y*-axes. Distal *X*-axes (right positive proximally, left positive distally) were calculated by crossing the distal *Y*- and *Z*-axes.

### Tarsometatarsal ACSs

Proximal and distal ACSs were made for the tarsometatarsi (Fig. A1E). Inertial axes were calculated for each model, with the least inertial axes serving as the long, *X*-axes (right positive distally, left positive proximally). The origins of the proximal ACSs were placed at the level of the furthest proximal extensions of the intercotylar eminence. The axes of intermediate inertia closely approximated the transverse axis of the tarsometatarsal cotyles and so were used for the proximal *Z*-axes (both sides positive to the left). Proximal *Y*-axes were the axes of greatest inertia (right positive caudally, left positive cranially). The distal ACSs were made by translating copies of the proximal ACSs to the centroid of each third tarsometatarsal condyle.

### Pelvic JCS

Yaw measured rotation of the pelvic ACS about a fixed, global vertical *Z*-axis, positive to the left. Roll designated rotation about the local pelvic *X*-axis, raising the right acetabulum relative to the left being positive. Pitch quantified rotation about a floating JCS *Y*-axis (always orthogonal to the yaw and roll axes), head up being positive.

### Hip JCSs

Each hip JCS was created from axes of the acetabular ACS and proximal femoral ACS. FE angle measured rotation about the *Z*-axis of the acetabular ACS, extension being positive. LAR angle measured rotation of a femur model about the *X*-axis of its proximal ACS, external LAR being positive. ABAD angle measured rotation about a floating *Y*-axis that remained orthogonal to the *Z*- and *X*-axes, abduction being positive. Hip translations measured the displacement of the femoral head centroid from the acetabular centroid along axes of the acetabular ACS.

### Knee JCSs

Axes from the distal femoral ACS and proximal tibiotarsal ACS established each knee JCS. Knee FE measured rotation about the *Z*-axis of the femoral condyles, extension being positive. LAR measured rotation of the tibiotarsal model about its axis of least inertia (the *X*-axis of its proximal ACS), external LAR being positive. ABAD measured rotation about a floating *Y*-axis that remained orthogonal to the *Z*- and *X*-axes, adduction being positive. Knee translations measured offset of the proximal tibiotarsal ACS relative to the distal femoral ACS.

### Ankle JCSs

Each ankle (intertarsal) JCS was created from axes of the distal tibiotarsal ACS and proximal tarsometatarsal ACS. Ankle FE measured rotation about the *Z*-axis of the tibial condyles, extension being positive. LAR measured rotation of the tarsometatarsal model about its axis of least inertia, the *X*-axis of its proximal ACS, external LAR being positive. ABAD measured rotation about a floating *Y*-axis that remained orthogonal to the *Z*- and *X*-axes, abduction being positive. Ankle translations measured offset of the proximal tarsometatarsal ACS relative to the distal tibiotarsal ACS.

### Reference pose

When all translations and rotations are zeroed, the pairs of ACSs contributing to each JCS are perfectly aligned (Fig. A2A,B). We call this the reference pose. Each limb is collapsed into a tight zig-zag configuration with the femoral long axes parallel to the pelvic long axis. The tibiotarsi and tarsometatarsi splay laterally as a result of the obliquity of the femoral condyles. For all but the pelvic ACS, the *X*- and *Z*-axes are oriented horizontally and the *Y*-axes are oriented vertically. Although not physically possible (bones interpenetrate), the reference pose is a useful starting point from which to interpret our graphs of 3D rotations about multiple joints in both limbs. Comparison of reference poses also assured us that our ACSs (and in turn our JCSs) were being calculated consistently among individual guineafowl.

### Acknowledgements

We thank Elizabeth Brainerd, David Baier and members of the Brown Morphology Group for their contributions to marker-based XROMM. We are grateful to Peter Falkingham, Ariel Camp, Erika Giblin and Angela Horner for assistance with experiments and to John Hutchinson, Danny Miranda and Mike Rainbow for guidance on joint coordinate systems. Kia Huffman helped with all aspects of the XMA Portal. Our conical carbide markers were based on a design by Farish Jenkins, Jr and William Amaral, with fabrication advice from Amy Davidson. We appreciate the thoughtful suggestions of two anonymous reviewers.

### Competing interests

The authors declare no competing financial interests.

### Author contributions

R.E.K., T.J.R. and S.M.G. all significantly contributed to study conception, experimental design, data collection and manuscript preparation. R.E.K. and S.M.G. performed the XROMM analysis.

### Funding

This work was supported by the US National Science Foundation [IOS-0925077, DBI-0552051, IOS-0840950, DBI-1262156], the W. M. Keck Foundation and the Bushnell Research and Education Fund.

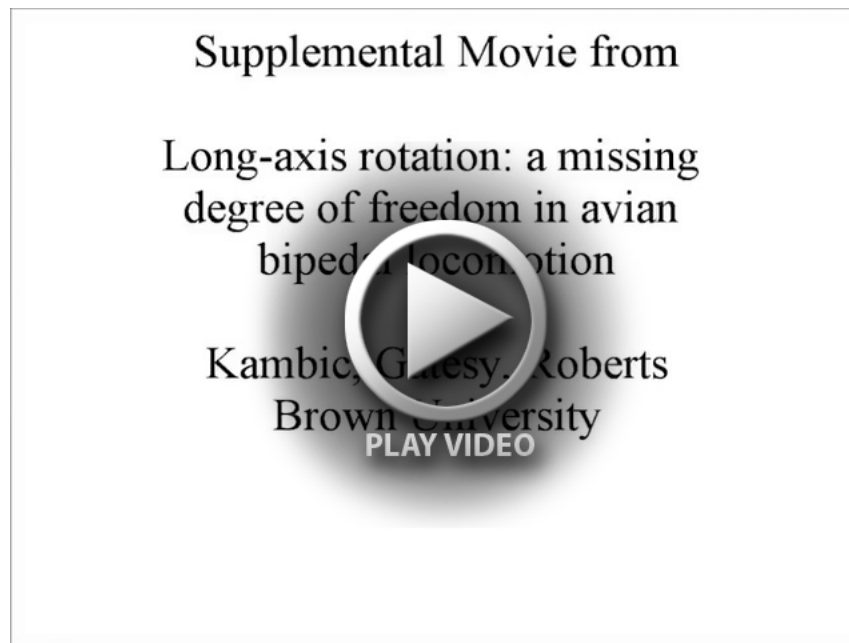
### Supplementary material

Supplementary material available online at <http://jeb.biologists.org/lookup/suppl/doi:10.1242/jeb.101428/-/DC1>

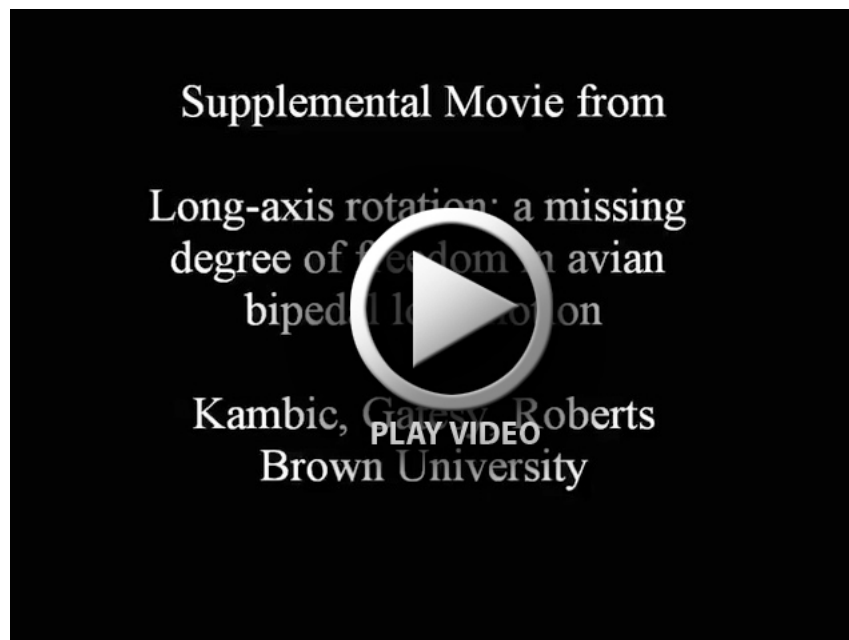
### References

- Abourachid, A. (2001). Kinematic parameters of terrestrial locomotion in cursorial (ratites), swimming (ducks), and striding birds (quail and guinea fowl). *J. Comp. Physiol. A* **131**, 113–119.
- Abourachid, A. and Renous, S. (2000). Bipedal locomotion in ratites (Paleognathiform) examples of cursorial birds. *Ibis* **142**, 538–549.
- Abourachid, A., Hackert, R., Herbin, M., Libourel, P. A., Lambert, F., Gioanni, H., Provini, P., Blazevic, P. and Hugel, V. (2011). Bird terrestrial locomotion as revealed by 3D kinematics. *Zoology* **114**, 360–368.
- Allen, V., Bates, K. T., Li, Z. and Hutchinson, J. R. (2013). Linking the evolution of body shape and locomotor biomechanics in bird-line archosaurs. *Nature* **497**, 104–107.
- Andrada, E., Rode, C. and Blickhan, R. (2013a). Grounded running in quails: simulations indicate benefits of observed fixed aperture angle between legs before touch-down. *J. Theor. Biol.* **335**, 97–107.
- Andrada, E., Nyakatura, J. A., Bergmann, F. and Blickhan, R. (2013b). Adjustments of global and local hindlimb properties during terrestrial locomotion of the common quail (*Coturnix coturnix*). *J. Exp. Biol.* **216**, 3906–3916.
- Besier, T. F., Sturnieks, D. L., Alderson, J. A. and Lloyd, D. G. (2003). Repeatability of gait data using a functional hip joint centre and a mean helical knee axis. *J. Biomech.* **36**, 1159–1168.
- Birn-Jeffery, A. V. and Daley, M. A. (2012). Birds achieve high robustness in uneven terrain through active control of landing conditions. *J. Exp. Biol.* **215**, 2117–2127.
- Blob, R. W. and Biewener, A. A. (2001). Mechanics of limb bone loading during terrestrial locomotion in the green iguana (*Iguana iguana*) and American alligator (*Alligator mississippiensis*). *J. Exp. Biol.* **204**, 1099–1122.
- Brainerd, E. L., Baier, D. B., Gatesy, S. M., Hedrick, T. L., Metzger, K. A., Gilbert, S. L. and Crisco, J. J. (2010). X-ray reconstruction of moving morphology (XROMM): precision, accuracy and applications in comparative biomechanics research. *J. Exp. Zool. A* **313**, 262–279.
- Brinkman, D. (1981). The hind limb step cycle of Iguana and primitive reptiles. *J. Zool.* **181**, 91–103.
- Cappozzo, A., Catani, F., Leardini, A., Benedetti, M. G. and Croce, U. D. (1996). Position and orientation in space of bones during movement: experimental artefacts. *Clin. Biomech.* **11**, 90–100.

- Carrano, M. T. (1998). Locomotion in non-avian dinosaurs: integrating data from hindlimb kinematics, in vivo strains, and bone morphology. *Paleobiology* **24**, 450-469.
- Clark, J. and Alexander, R. MN. (1975). Mechanics of running in quail (*Coturnix*). *J. Zool.* **176**, 87-113.
- Coombs, W. P., Jr (1978). Theoretical aspects of cursorial adaptations in dinosaurs. *Q. Rev. Biol.* **53**, 393-418.
- Cracraft, J. (1971). The functional morphology of the hind limb of the domestic pigeon, *Columba livia*. *Bulletin of the American Museum of Natural History* **144**, 171-268.
- Crisco, J. J. and McGovern, R. D. (1997). Efficient calculation of mass moments of inertia for segmented homogeneous three-dimensional objects. *J. Biomech.* **31**, 97-101.
- Daley, M. A. and Biewener, A. A. (2006). Running over rough terrain reveals limb control for intrinsic stability. *Proc. Natl. Acad. Sci. USA* **103**, 15681-15686.
- Daley, M. A., Felix, G. and Biewener, A. A. (2007). Running stability is enhanced by a proximo-distal gradient in joint neuromechanical control. *J. Exp. Biol.* **210**, 383-394.
- Dawson, M. M., Metzger, K. A., Baier, D. B. and Brainerd, E. L. (2011). Kinematics of the quadrate bone during feeding in mallard ducks. *J. Exp. Biol.* **214**, 2036-2046.
- Dial, K. P., Goslow, G. E., Jr and Jenkins, F. A., Jr (1991). The functional anatomy of the shoulder of the European starling (*Sturnus vulgaris*). *J. Morphol.* **207**, 327-344.
- Ellerby, D. J. and Marsh, R. L. (2010). The mechanical function of linked muscles in the guinea fowl hind limb. *J. Exp. Biol.* **213**, 2201-2208.
- Gatesy, S. M. (1990). Caudofemoral musculature and the evolution of theropod locomotion. *Paleobiology* **16**, 170-186.
- Gatesy, S. M. (1999). Guineafowl hind limb function I: cineradiographic analysis and speed effects. *J. Morphol.* **240**, 115-125.
- Gatesy, S. M. and Biewener, A. A. (1991). Bipedal locomotion: effects of speed, size and limb posture in birds and humans. *J. Zool. (Lond.)* **224**, 127-147.
- Gatesy, S. M., Baier, D. B., Jenkins, F. A. and Dial, K. P. (2010). Scientific roscoping: a morphology-based method of 3-D motion analysis and visualization. *J. Exp. Zool. A* **313**, 244-261.
- Gidmark, N. J., Konow, N., Lopresti, E. and Brainerd, E. L. (2013). Bite force is limited by the force-length relationship of skeletal muscle in black carp, *Mylopharyngodon piceus*. *Biol. Lett.* **9**, 20121181.
- Goetz, J. E., Derrick, T. R., Pedersen, D. R., Robinson, D. A., Conzemius, M. G., Baer, T. E. and Brown, T. D. (2008). Hip joint contact force in the emu (*Dromaius novaehollandiae*) during normal level walking. *J. Biomech.* **41**, 770-778.
- Gosnell, W. C., Butcher, M. T., Maie, T. and Blob, R. W. (2011). Femoral loading mechanics in the Virginia opossum, *Didelphis virginiana*: torsion and mediolateral bending in mammalian locomotion. *J. Exp. Biol.* **214**, 3455-3466.
- Good, E. S. and Suntay, W. J. (1983). A joint coordinate system for the clinical description of three-dimensional motions: application to the knee. *J. Biomech. Eng.* **105**, 136-144.
- Hancock, J. A., Stevens, N. J. and Biknevičius, A. R. (2007). Whole-body mechanics and kinematics of terrestrial locomotion in the elegant-crested tinamou *Eudromia elegans*. *Ibis* **149**, 605-614.
- Henry, H. T., Ellerby, D. J. and Marsh, R. L. (2005). Performance of guinea fowl *Numida meleagris* during jumping requires storage and release of elastic energy. *J. Exp. Biol.* **208**, 3293-3302.
- Hertel, F. and Campbell, K. E., Jr (2007). The antitrochanter of birds: form and function in balance. *Auk* **124**, 789-805.
- Hugel, V., Hackert, R. and Abourachid, A. (2011). Kinematic modeling of bird locomotion from experimental data. *IEEE Trans. Robot.* **27**, 185-200.
- Hutchinson, J. R. and Allen, V. (2009). The evolutionary continuum of limb function from early theropods to birds. *Naturwissenschaften* **96**, 423-448.
- Hutchinson, J. R. and Gatesy, S. M. (2000). Adductors, abductors, and the evolution of archosaur locomotion. *Paleobiology* **26**, 734-751.
- Jacobson, R. D. and Hollyday, M. (1982). A behavioral and electromyographic study of walking in the chick. *J. Neurophysiol.* **48**, 238-256.
- Jayne, B. C. and Irschick, D. J. (1999). Effects of incline and speed on the three-dimensional hindlimb kinematics of a generalized iguanian lizard (*Dipsosaurus dorsalis*). *J. Exp. Biol.* **202**, 143-159.
- Jenkins, F. A., Jr, Dial, K. P. and Goslow, G. E., Jr (1988). A cineradiographic analysis of bird flight: the wishbone in starlings is a spring. *Science* **241**, 1495-1498.
- Jindrich, D. L., Besier, T. F. and Lloyd, D. G. (2006). A hypothesis for the function of braking forces during running turns. *J. Biomech.* **39**, 1611-1620.
- Jindrich, D. L., Smith, N. C., Jaspers, K. and Wilson, A. M. (2007). Mechanics of cutting maneuvers by ostriches (*Struthio camelus*). *J. Exp. Biol.* **210**, 1378-1390.
- Johnston, R. M. and Bekoff, A. (1992). Constrained and flexible features of rhythmical hindlimb movements in chicks: kinematic profiles of walking, swimming and airstepping. *J. Exp. Biol.* **171**, 43-66.
- Kaiser, J., Bradford, R., Johnson, K., Wieben, O. and Thelen, D. G. (2013). Measurement of tibiofemoral kinematics using highly accelerated 3D radial sampling. *Magn. Reson. Med.* **69**, 1310-1316.
- Main, R. P. and Biewener, A. A. (2007). Skeletal strain patterns and growth in the emu hindlimb during ontogeny. *J. Exp. Biol.* **210**, 2676-2690.
- Manion, B. L. (1984). *The Effects of Size and Growth on the Hindlimb Locomotion in the Chicken*. PhD thesis, University of Illinois at Chicago, IL, USA.
- Markolf, K. L., Mensch, J. S. and Amstutz, H. C. (1976). Stiffness and laxity of the knee – the contributions of the supporting structures. A quantitative *in vitro* study. *J. Bone Joint Surg. Am.* **58**, 583-594.
- Miranda, D. L., Rainbow, M. J., Leventhal, E. L., Crisco, J. J. and Fleming, B. C. (2010). Automatic determination of anatomical coordinate systems for three-dimensional bone models of the isolated human knee. *J. Biomech.* **43**, 1623-1626.
- Nowroozi, B. N. and Brainerd, E. L. (2013). X-ray motion analysis of the vertebral column during the startle response in striped bass, *Morone saxatilis*. *J. Exp. Biol.* **216**, 2833-2842.
- Nyakatura, J. A., Andrada, E., Grimm, N., Weise, H. and Fischer, M. S. (2012). Kinematics and center of mass mechanics during terrestrial locomotion in northern lapwings (*Vanellus vanellus*, Charadriiformes). *J. Exp. Zool. A* **317**, 580-594.
- Piazza, S. J. and Cavanagh, P. R. (2000). Measurement of the screw-home motion of the knee is sensitive to errors in axis alignment. *J. Biomech.* **33**, 1029-1034.
- Provine, P., Goupil, P., Hugel, V. and Abourachid, A. (2012). Walking, paddling, waddling: 3D kinematics anatine locomotion (*Collonetta leucophrys*). *J. Exp. Zool. A* **317**, 275-282.
- Reilly, S. M. (2000). Locomotion in the quail (*Coturnix japonica*): the kinematics of walking and increasing speed. *J. Morphol.* **243**, 173-185.
- Reilly, S. M., Willey, J. S., Biknevičius, A. R. and Blob, R. W. (2005). Hindlimb function in the alligator: integrating movements, motor patterns, ground reaction forces and bone strain of terrestrial locomotion. *J. Exp. Biol.* **208**, 993-1009.
- Reinschmidt, C., van den Bogert, A. J., Nigg, B. M., Lundberg, A. and Murphy, N. (1997). Effect of skin movement on the analysis of skeletal knee joint motion during running. *J. Biomech.* **30**, 729-732.
- Roberts, T. J. (2001). Muscle force and stress during running in dogs and wild turkeys. *Bull. Mus. Comp. Zool.* **156**, 283-295.
- Roberts, T. J. and Scales, J. A. (2002). Mechanical power output during running accelerations in wild turkeys. *J. Exp. Biol.* **205**, 1485-1494.
- Roberts, T. J. and Scales, J. A. (2004). Adjusting muscle function to demand: joint work during acceleration in wild turkeys. *J. Exp. Biol.* **207**, 4165-4174.
- Rosset, A., Spadola, L., Pysher, L. and Ratib, O. (2006). Informatics in radiology (infoRAD): Navigating the fifth dimension: innovative interface for multidimensional multimodality image navigation. *Radiographics* **26**, 299-308.
- Rubenson, J. and Marsh, R. L. (2009). Mechanical efficiency of limb swing during walking and running in guinea fowl (*Numida meleagris*). *J. Appl. Physiol.* **106**, 1618-1630.
- Rubenson, J., Lloyd, D. G., Besier, T. F., Heliams, D. B. and Fournier, P. A. (2007). Running in ostriches (*Struthio camelus*): three-dimensional joint axes alignment and joint kinematics. *J. Exp. Biol.* **210**, 2548-2562.
- Rubenson, J., Lloyd, D. G., Heliams, D. B., Besier, T. F. and Fournier, P. A. (2011). Adaptations for economical bipedal running: the effect of limb structure on three-dimensional joint mechanics. *J. R. Soc. Interface* **8**, 740-755.
- Rylander, M. K. and Bolen, E. G. (1974). Analysis and comparison of gaits in whistling ducks (*Dendrocygna*). *Wilson Bulletin* **86**, 237-245.
- Scanlan, S. F., Lai, J., Donahue, J. P. and Andriacchi, T. P. (2012). Variations in the three-dimensional location and orientation of the ACL in healthy subjects relative to patients after transtibial ACL reconstruction. *J. Orthop. Res.* **30**, 910-918.
- Sigmund, L. (1959). Mechanik und anatomische Grundlagen der Fortbewegung bei wasserralle (*Rallus aquaticus* L.), teichhuhn (*Gallinula chloropus* L.) und blasshuhn (*Fulica atra* L.). *J. Ornithol.* **100**, 3-24.
- Smith, N. C., Jaspers, K. J. and Wilson, A. M. (2010). Ontogenetic scaling of locomotor kinetics and kinematics of the ostrich (*Struthio camelus*). *J. Exp. Biol.* **213**, 1347-1355.
- Stoessel, A. and Fischer, M. S. (2012). Comparative intralimb coordination in avian bipedal locomotion. *J. Exp. Biol.* **215**, 4055-4069.
- Tashman, S. and Anderst, W. (2003). In-vivo measurement of dynamic joint motion using high speed biplane radiography and CT: application to canine ACL deficiency. *J. Biomech. Eng.* **125**, 238-245.
- Troy, K. L., Brown, T. D. and Conzemius, M. G. (2009). Contact stress distributions on the femoral head of the emu (*Dromaius novaehollandiae*). *J. Biomech.* **42**, 2495-2500.
- Verstappen, M., Aerts, P. and Van Damme, R. (2000). Terrestrial locomotion in the black-billed magpie: kinematic analysis of walking, running and out-of-phase hopping. *J. Exp. Biol.* **203**, 2159-2170.
- Wu, G. and Cavanagh, P. R. (1995). ISB recommendations for standardization in the reporting of kinematic data. *J. Biomech.* **28**, 1257-1261.
- Wu, G., Siegler, S., Allard, P., Kirtley, C., Leardini, A., Rosenbaum, D., Whittle, M., D'Lima, D. D., Cristofolini, L., Witte, H. et al.; Standardization and Terminology Committee of the International Society of Biomechanics; International Society of Biomechanics (2002). ISB recommendation on definitions of joint coordinate system of various joints for the reporting of human joint motion – part I: ankle, hip, and spine. *J. Biomech.* **35**, 543-548.
- Wu, G., van der Helm, F. C., Veeger, H. E., Makhssous, M., Van Roy, P., Anglin, C., Nagels, J., Karduna, A. R., McQuade, K., Wang, X. et al.; International Society of Biomechanics (2005). ISB recommendation on definitions of joint coordinate systems of various joints for the reporting of human joint motion – Part II: shoulder, elbow, wrist and hand. *J. Biomech.* **38**, 981-992.
- Zatsiorsky, V. M. (1998). *Kinematics of Human Motion*. Champaign, IL: Human Kinetics.



**Movie 1. Overhead views of the five maneuvers discussed in this study.** Bones disappear as they leave the view of one or both X-rays. Sequences are not to scale with each other.



**Movie 2. Three sequences of XROMM animation from a complex maneuvering trial.** First sequence: video from X-ray system 2 of a guineafowl maneuvering within the X-ray volume. Note the conical markers implanted in the pelvis and hind limb bones. Animated bone models appear over the images and confirm the accuracy of the reconstructed motion. Second sequence: the same maneuvers viewed with a standard light camera. The animated models are correctly registered as if the viewer can see through soft tissue to the bones beneath. Third sequence: the entire maneuvering trial (see Fig. 4) with the limbs moving relative to a stable pelvis, illustrating the variety of non-sagittal poses and contribution of LAR.